Journal of Materials Chemistry C

ROYAL SOCIETY OF CHEMISTRY

PAPER

View Article Online
View Journal | View Issue

Cite this: J. Mater. Chem. C, 2023, 11, 6220

Effect of Mn^{2+} doping on exciton recombination and carrier trapping in the Cs_2CdCl_4 metal halide†

Dayu Huang,[ab] Ziyong Cheng,[ab] Qiuyun Ouyang,*[a] Hongzhou Lian*[ab] and Jun Lin *[ab]

Received 20th March 2023,
Accepted 15th April 2023

DOI: 10.1039/d3tc00982c

rsc.li/materials-c

The lattice defects that occur in material preparation processes are closely related to carrier migration. The carrier migration can be regulated by artificially modulating the defects to improve the luminescence performance, which is important for the development and application of luminescent materials. Here, we achieved a 3.29-fold increase in the high-temperature luminescence intensity by introducing Mn^{2+} to generate Cl vacancy defects in Cs_2CdCl_4. Due to thermally induced electron de-trapping, Cs_2CdCl_4:Mn^{2+} also displays anti-thermal quenching (ATQ) behavior and good thermal quenching resistance (329% at 175 °C). The increase in the photoionization effect and de-trapping of the captured electrons from shallow trap states were appropriately attributed to this exceptional phenomenon, based on thermoluminescence (TL) analysis. Based on comprehensive optical characterization, thermoluminescence and temperature-dependent X-ray diffraction (XRD), we reveal that the Cl vacancy trap state generated by Mn doping is the reason for the enhanced PL in air. The discovery of these materials helps to better understand the optical properties of all-inorganic perovskites.

1. Introduction

The study of metal halides has grown exponentially due to their excellent photoelectric properties.[1–24] One aspect of this work involves replacing Pb in the metal halide with other metals to form materials with different chemical or physical properties or better stability than Pb halide perovskites.[25–30] The characteristic 3D double perovskite structure of $CsPbX_3$ (X = Cl, Br, and I) is retained, that is, the Pb^{2+} cation in the compound is replaced by monovalent and trivalent cations in pairs, as described by the $Cs_2M^+M'^+X_6$ (X = Cl, Br, and I) formula unit.[31–38] Another research direction is to explore low-dimensional perovskites with metal halide octahedra forming 2D structures or isolated 0D units. In 2D perovskites, layers composed of metal halide octahedral and monovalent cations appear alternately. In this structure, the size limitation of monovalent cation selection in 3D perovskites is greatly relaxed, such that hybrid 2D perovskites can be formed in which the 2D metal halide layers are alternately arranged with organic monovalent cation layers of different sizes.[39,40] Such organic–inorganic hybrid perovskites exhibit excellent optical properties, such as a tunable emission range, a narrow emission line width and a high photoluminescence quantum yield (PLQY). Among all the possible arrangements of metal halide octahedral layers, there is the unique Ruddlesden–Popper (RP) phase, which has attracted extensive attention due to its chemical diversity, stability and properties that are similar to 3D structures.[40,41] The RP phase is in the stoichiometric ratio of the formula unit A_2MX_4 (A and X = monovalent or divalent ions; M = metal cations), which are composed of co-angular MX_6 octahedral sheets stacked in an ABAB sequence along the *c* axis. Such a structure, *e.g.*, oxide Sr_2TiO_4, was first discovered by Ruddlesden and Popper.[42] In the past century, halide-based RP phases have attracted much attention due to their excellent photoelectric properties, and are considered to be a new class of semiconductor materials. The host Cs_2CdCl_4 in this paper has also been identified to have the same RP structure.[43] Koshimizu's group reported that Cs_2CdCl_4 as an X-ray scintillator material can emit light by doping Sb^{3+} or Tl^+.[44] Among them, the prominent feature of Cs_2CdCl_4:Sb^{3+} is that there is only a single emission band. The maximum emission peak is located at 516 nm. However, compared with the corresponding bulk compounds, RP phase materials exhibit unique physical and photoelectric properties as colloidal nanocrystals. The research of Locardi's group involved the formation of the Cs_2CdCl_4:Sb^{3+} RP phase as colloidal nanocrystals.[45] Under UV excitation, Cs_2CdCl_4:Sb^{3+} has a strong cyan emission. Doping transition metals into perovskites is a unique strategy to expand the family of perovskite materials. However, undoped materials

[a] Key Laboratory of In-Fiber Integrated Optics, Ministry Education of China, and College of Physics and Opotoelectronic Engineering, Harbin Engineering University, Harbin 150001, China. E-mail: qyouyang@hrbeu.edu.cn, hzlian@ciac.ac.cn, jlin@ciac.ac.cn
[b] State Key Laboratory of Rare Earth Resource Utilization, Changchun Institute of Applied Chemistry, Chinese Academy of Sciences, Changchun 130022, P. R. China

† CCDC 2235089. For crystallographic data in CIF or other electronic format see DOI: https://doi.org/10.1039/d3tc00982c

cannot change their optical and electronic properties. Based on the unique properties of Cd-based halide perovskites, their photoelectric properties were studied under the activation of photoluminescence center signals. It is proved that the doping effect is crucial for photon upconversion and a higher excited state emission. So far, Mn^{2+} activated luminescent materials exhibit high thermal quenching due to strong electron–lattice coupling during heating. Therefore, it is a meaningful work to develop Mn^{2+} ion doped perovskites with high thermal stability and high efficiency for lighting applications.

In this work, we studied the relationship between radiative exciton recombination and carrier trapping on the surface of the Cs_2CdCl_4:Mn^{2+} perovskite crystal *via* high temperature spectra. It is found that the photoluminescence (PL) intensity of the Cs_2CdCl_4:Mn^{2+} crystal can be increased 3.29 fold by increasing the temperature from room temperature to 175 °C. Based on comprehensive steady-state and dynamic optical characterizations, we attribute the enhanced PL with increasing temperature to the reduced density of states associated with Cl vacancies near the crystal surface. We found that the carriers trapped by Cl vacancies are activated at high temperature, contributing to the PL intensity. Therefore, we speculate that the trap density of the Cs_2CdCl_4:Mn^{2+} crystal is more than that of the Cs_2CdCl_4 crystal. It is worth noting that high temperature is detrimental to the performance of perovskite LEDs. Our results provide a new means of improving the stability of devices based on all-inorganic perovskites, and highlight the interesting photoelectric properties of Cs_2CdCl_4:Mn^{2+} crystals due to high temperature.

2. Experimental

2.1 Chemicals

All chemicals were used without further purification: CdO (cadmium oxide, Aladdin), CsCl (cesium chloride, Aladdin), HCl (hydrochloric acid, 36–38%) aqueous solution, *N*,*N*-dimethylformamide (Aladdin), and $(CH_3COO)_2Mn$ (manganous acetate, Aladdin). All reactions were performed under ambient conditions.

2.2 Synthesis of Cs_2CdCl_4 and Cs_2CdCl_4:*x*Mn^{2+}

Cs_2CdCl_4 and Cs_2CdCl_4:Mn^{2+} were synthesized *via* a hydrothermal method. For the Cs_2CdCl_4 host, CsCl (4 mmol) and CdO (1 mmol) were added to a 25 mL Teflon-lined autoclave. Then, 3 mL of HCl aqueous solution was added to the Teflon-lined autoclave followed by 3 mL DMF, and the autoclave was heated at 150 °C for 2 h before being cooled slowly at 2 °C h^{-1} to room temperature. Finally, the obtained single crystal particles were washed two times with ethanol and dried at 80 °C for 1 h in an oven. For Cs_2CdCl_4:Mn^{2+}, $(CH_3COO)_2Mn$ (0.1 mmol) was added to the Teflon-lined autoclave, and other steps are the same.

2.3 Characterization

The single-crystal X-ray diffraction (SCXRD) data were recorded using a Bruker Apex II CCD diffractometer with X-ray Mo Kα radiation (λ = 0.71073 Å). A suitable single crystal was selected and kept at room temperature during data collection. Data reduction, experimental absorption correction, and cell refinement were obtained using the APEX3software package. Using Olex2 software, the structure was solved by the ShelXT structural solution program using the Intrinsic Phasing method and refined by the ShelXL refinement package using least-squares minimization. Phase identification was confirmed through X-ray diffraction using a D8 Focus diffractometer (Bruker) with Cu-Kα radiation (λ = 1.5405 Å). The diffuse reflectance spectra (DRS) were obtained using a UV-visible diffuse reflectance spectrophotometer (UV-2550 PC, Shimadzu Corporation, Japan). TEM was carried out using a FEI Tecnai G2S-Twin microscope with a field-emission gun operating at 200 kV. Photoluminescence (PL) spectra and temperature-dependent PL spectra (from −180 to 100 °C) were obtained using a fluorescence spectrophotometer with a 450 W xenon lamp as the excitation source equipped with a temperature controller (Edinburgh Instruments FLS-920). The photoluminescence quantum yield (PLQY) values were collected using an absolute PL quantum yield measurement system equipped with a temperature controller (Hamamatsu Photonics K.K., C9920-02 Japan). A LTTL-3DS spectrometer was used to record the two-dimensional (2D) thermoluminescence (TL) curves at a heating rate of 2 K s^{-1}. Thermogravimetric studies were carried out using a simultaneous thermal analyzer (STA 449 F3).

3. Results and discussion

High-quality Cs_2CdCl_4:Mn^{2+} perovskite crystals were prepared using a hydrothermal technique. The results of powder X-ray diffraction (PXRD) tests are consistent with those of single-crystal X-ray diffraction (SCXRD), and the Cs_2CdCl_4:Mn^{2+} crystal has a clear *I*4/*m* space group (Fig. 1a). Table 1 lists the detailed structural parameters. According to Fig. 1b, the structure units of Cs_2CdCl_4 are built up of $[CdCl_6]^{4-}$ and $[CsCl_9]^{8-}$ polyhedra, in which Mn^{2+} ions are known to selectively occupy the 6-coordinated Cd^{2+} sites because of their similar valence state and ionic radii ($R_{Cd^{2+}}$ = 0.95 Å and $R_{Mn^{2+}}$ = 0.67 Å). The XPS outcomes are displayed in Fig. 1c. In particular, the peak of Mn^{2+} binding energy at 653.04 eV corresponds to the 2p orbital of Mn^{2+}. The XPS peak position of Mn^{2+} is consistent with many previous reports,[19] demonstrating the successful introduction of Mn^{2+}, and the signal peaks of Cs, Cd, C and Cl are well shown. From the EPR spectrum of Mn^{2+} (Fig. 1d) under the influence of an external magnetic field, it is further confirmed that Mn^{2+} exists in the material and that just one site in the lattice is suitable for Mn^{2+}. A weak Mn–Mn dipole contact also exists.[46]

Fig. 2a displays the UV/Vis diffuse reflectance (DR) spectrum of Cs_2CdCl_4:Mn^{2+}. Here, Cs_2CdCl_4:Mn^{2+} exhibits several absorption sites and an indirect bandgap (Fig. 2b). Indeed, under observation with the naked eye, Cs_2CdCl_4:Mn^{2+} exhibited yellow emission under UV irradiation, which is clearly brighter than that of pristine Cs_2CdCl_4. The host's own luminescence is very weak or even invisible to the naked eye (Fig. 2c). After Mn^{2+} doping, the Mn^{2+} d–d emission corresponding to the spin-forbidden $^4T_1 \rightarrow {}^6A_1$

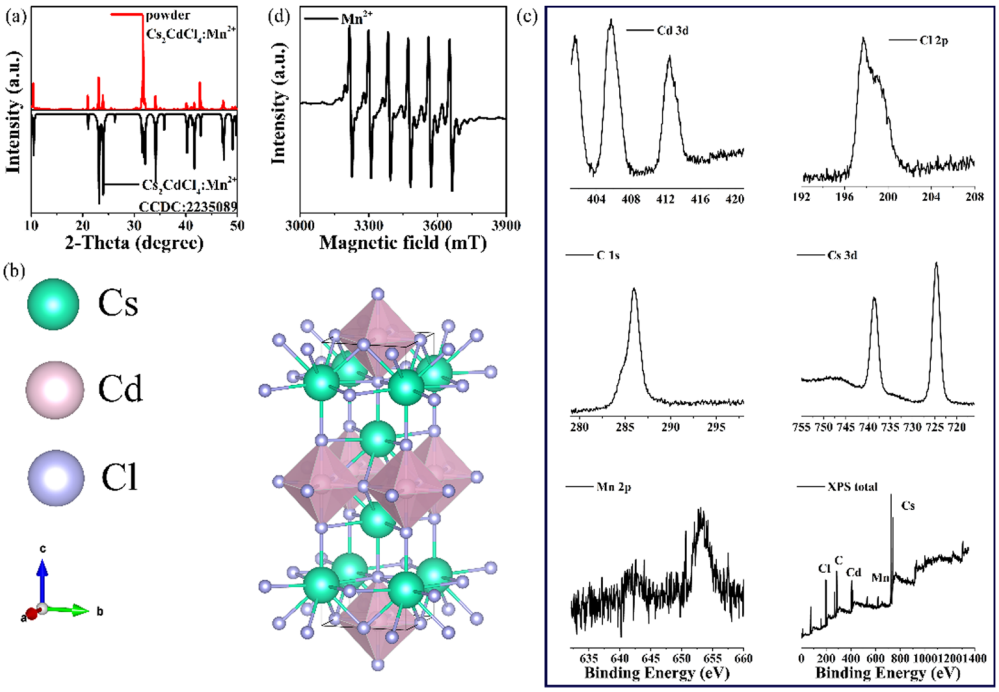

Fig. 1 (a) X-ray diffraction pattern of the Cs_2CdCl_4:Mn^{2+} perovskite crystal, showing the *I*4/*m* space group that coincides well with CCDC 2235089 (a = b = 5.2464 Å, c = 16.854 Å, $\alpha = \beta = \gamma = 90°$). (b) Crystal structure of Cs_2CdCl_4. (c) XPS spectra corresponding to Cs_2CdCl_4, Cs, Cd, Mn, C and Cl. (d) EPR spectrum of Cs_2CdCl_4:Mn^{2+}.

Table 1 Structural data of single crystal Cs_2CdCl_4:Mn^{2+}

Structural parameter	Cs_2CdCl_4:Mn^{2+}
a	5.2464 Å
b	5.2464 Å
c	16.854 Å
Volume	463.9 Å^3
Space group	*I*4/*m*
Z	4
h	7
k	7
l_{max}	23
R (reflections)	0.0663
wR_2 (reflections)	0.1851
CCDC	2235089

transition can be observed as a broadband yellow emission peak at around 585 nm with excitation at 417 nm (Fig. 2d). The emission bands of these samples share many solitary excitation bands at 250–325, 325–375, 417, and 475–550 nm, which perhaps belong to a charge transfer band and electronic transitions from $^6A_{1g}(S)$ to the excited state. The corresponding excitation spectrum is shown in Fig. 2d. The distinct transitions show different excitation peaks. The excitation peak at 250–325 nm belongs to the charge transfer band of the host. The excitation peak at 325–375 nm is attributed to the $^4E_g(^4D)/^4T_{2g}(^4D)$–$^6A_1$ transition. The $^4E_{2g}(^4G)/^4T_{2g}(^4G)/^4A_1$-$(^4G)$–$^6A_1$ transition is responsible for the excitation peak at 417 nm. Moreover, the $^4T_1(^4G)$–$^6A_1$ transition is involved in the excitation peak at 475–550 nm.

Fig. 2e and f present photographs of the luminescence of the samples under visible light and ultraviolet light, respectively. The size and the yellow emission of the Cs_2CdCl_4:Mn^{2+} are clearly shown. In addition, grinding the single crystal into powder does not affect the luminescence intensity of the sample. The PLQY of the material can reach 90%.

In order to study the temperature dependence of the photoluminescence of the Cs_2CdCl_4:Mn^{2+} crystal, we monitored the crystal luminescence at high temperature. Fig. 3a shows the PL spectra of the Cs_2CdCl_4:Mn^{2+} crystal excited at 275 nm at different temperatures. Surprisingly, as shown in Fig. 3c, the PL intensity at high temperature increases by 3.29 fold ($I_{(175°C)}$ = $3.29I_{(25°C)}$, where $I_{(175°C)}$ is the integrated intensity at 175 °C, and $I_{(25°C)}$ is the integrated intensity at 25 °C). As shown in Fig. 3a, the PL peak of the Cs_2CdCl_4:Mn^{2+} crystal shows a clear enhancement and a blue shift as the temperature is increased. The blue shift of the emission peak at high temperature is because the crystal field strength of the material becomes weaker, which is generally accepted (Fig. 3b). It can be seen that the PL intensity decreases slowly before −100 °C, and then begins to increase slowly. As the temperature continues to rise, between 75 and 175 °C, the luminescence intensity increases rapidly and reaches the strongest state. Such a heating process can be repeated many times without any signs of change (Fig. 3d).

In order to obtain the mechanism of the temperature-dependent PL, it is necessary to understand the reasons for the PL enhancement of the Cs_2CdCl_4:Mn^{2+} perovskite crystals at high temperature, which is crucial for further analysis. In general, two possible scenarios can be assumed to explain the higher PL intensity at temperatures higher than room temperature. (1) The PL origin is related to the non-intrinsic radiation defect state, and the defect concentration increases at high temperature. This has recently been reported, and energy transfer from the trap state to

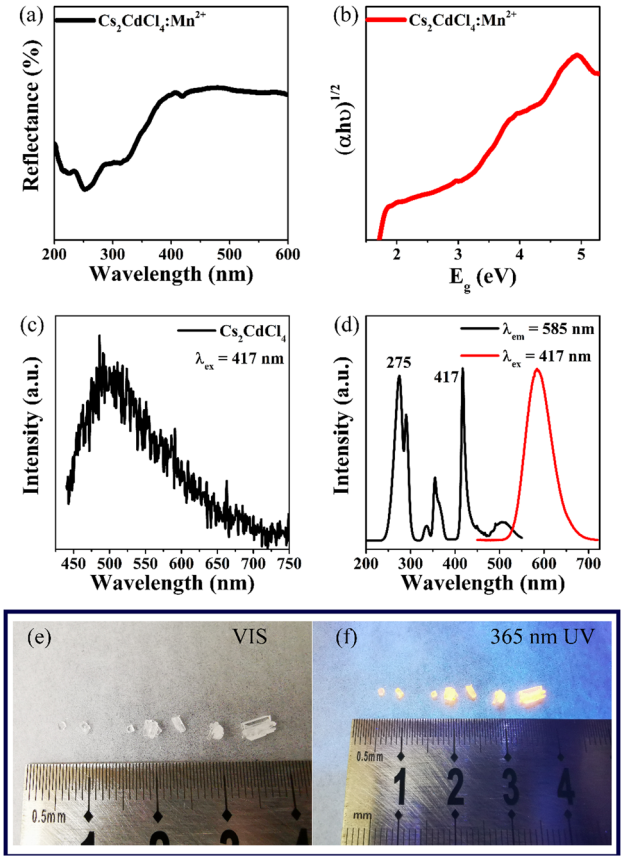

Fig. 2 (a) UV-vis reflectance spectra for Cs_2CdCl_4:Mn^{2+}. (b) Relationship between $[\alpha h\nu]^{1/2}$ and photon energy $h\nu$, showing indirect band gaps of Cs_2CdCl_4:Mn^{2+}. (c) PL spectrum of Cs_2CdCl_4. (d) PLE and PL spectrum of Cs_2CdCl_4:Mn^{2+}. (e and f) Photographs of single-crystal Cs_2CdCl_4:Mn^{2+} samples under visible and ultraviolet light illumination.

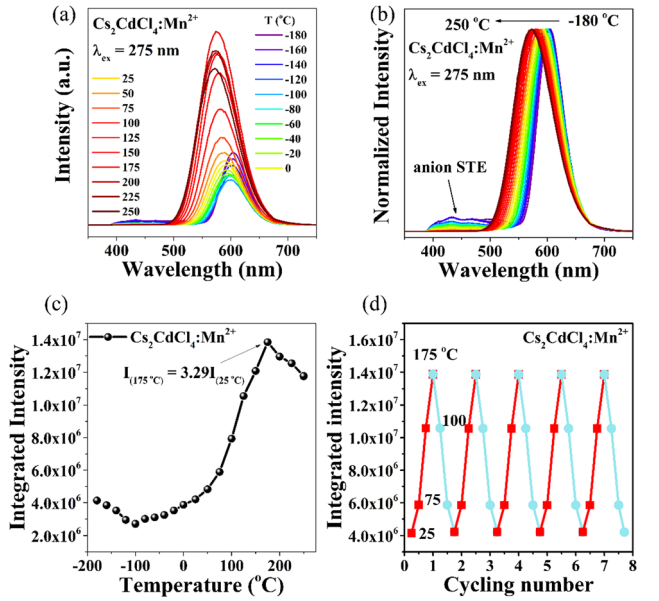

Fig. 3 (a) Temperature-dependent PL spectra of Cs_2CdCl_4:Mn^{2+}. (b) Normalized intensity of Cs_2CdCl_4:Mn^{2+} at different temperatures. (c) Integrated intensity of Cs_2CdCl_4:Mn^{2+} at different temperatures. (d) Cyclic heating test diagram from room temperature to 175 °C.

Mn^{2+} has been observed at high temperatures.[47] (2) If the PL originates from intrinsic interband or exciton recombination, it is necessary to verify the reduction of non-radiative recombination centers at high temperature. However, the luminescence enhancement is clearly not due to the decrease of the radiation centers, but the increase in the energy transfer path to Mn^{2+} at high temperature. Since significant self-trapped exciton (STE) emission can be observed at low temperature, the whole temperature-rise process refers to multiple photophysical behaviors.

First, we observe the normal emission intensity of Cs_2CdCl_4:Mn^{2+} in the region from −180 to −100 °C ($I_{-180°C}$ to $I_{-100°C}$) as shown Fig. 3c. This is initially used to return to the ground state radiation transition energy due to the phonon vibration loss, that is, thermal quenching behavior. Defect levels are not involved during this low-temperature process due to the lack of effective thermal activation energy. In region II (from −80 to 250 °C), the emission intensity at 175 °C is 329% of that at 20 °C. Nonetheless, Cs_2CdCl_4:Mn^{2+} exhibits the zero-thermal quenching phenomenon close to the working temperature of the LED chip, indicating its practical application potential. Generally, electron–phonon coupling becomes stronger and leads to the loss of luminescence intensity at high temperature. Hence, the thermal quenching and thermo-stimulated radiation dynamic process may form a competitive relationship to affect the luminescence intensity. Our initial hypothesis was that the STE energy of the host was transferred to Mn^{2+}; however, since the STE luminescence is so faint, it is hard to double the luminescence of Mn^{2+}.

Through XPS, we discovered an intriguing phenomenon in which the signal peaks of Cl in Cs_2CdCl_4 and Cl in Cs_2CdCl_4:Mn^{2+} moved and expanded significantly (Fig. 4a and b). The material itself has Cl^- vacancy defects, and the introduction of Mn^{2+} can control the Cl^- vacancy within a certain range, thereby maintaining stability at high temperature. Due to the high temperature, excessive Cl vacancy defects will lead to luminescence quenching. Therefore, the introduction of Mn avoids a large number of Cl vacancies at high temperatures and maintains a relatively balanced Cl vacancy ratio, which significantly enhances the anti-thermal quenching of Mn^{2+}. This is because a large number of Cl defects will bring about a large number of non-radiative complexes. This is the reason why we observe the anti-thermal quenching effect at high temperature.

To test the hypothesis proposed above, we obtained the following series of high temperature material characterization data. The material's luminous phase did not change at high temperatures, according to high temperature XRD (Fig. 4c). The TG curve proves that the quality of the sample does not change with the increase in temperature. The water adsorbed by the sample is lost (Fig. 4d). Subsequently, we examined the material's PLQY at different temperatures and discovered that, in addition to the PLQY of the material increasing at high temperatures, the absorption also increased, reaching a maximum before then declining (Table 2). The trend in the temperature-dependent quantum yield is similar to that of the temperature-dependent luminescence. The luminescence of the material is

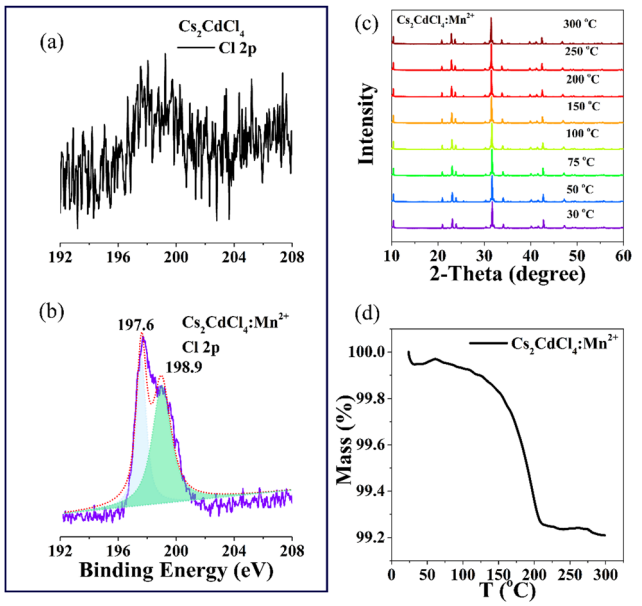

Fig. 4 XPS spectrum of Cl in (a) Cs_2CdCl_4 and (b) Cs_2CdCl_4:Mn^{2+}. (c) Temperature-dependent XRD patterns. (d) TG curve of Cs_2CdCl_4:Mn^{2+}.

enhanced with the increase in temperature. It is further proved that the luminescence of the material is indeed enhanced at high temperature, which is very beneficial for practical applications of the material.

In the information that follows, we demonstrate that the evidence points to the presence of several traps. Initially, a certain depth of lattice disorder is seen on the surface of the particles, probably as a result of the substitution of Mn^{2+} ions (Fig. 5a). Hence, the above finding indicated that the Cl vacancies, as electron trapping and storing sites, contributed to the enhanced emission intensity. To further support this view, the thermoluminescence (TL) glow curve, as a powerful tool to investigate the trapping state, was employed. Five trap levels were located between 300 and 600 K at various depths (Fig. 5b). $E = T_m/500$, where E is the average trap depth and T_m is the temperature corresponding to the peak position, is the empirical formula of Urbach.[48] The computed trap depths are 0.68, 0.74, 0.86, 0.99 and

Table 2 Temperature-dependent PLQY and absorption data for Cs_2CdCl_4:Mn^{2+}

Temperature (°C)	Quantum yield	Absorption
25	0.90	0.36
40	0.91	0.37
55	0.92	0.38
70	0.92	0.385
85	0.92	0.389
100	0.93	0.391
115	0.94	0.393
130	0.94	0.396
145	0.94	0.398
160	0.95	0.41
175	0.95	0.412
190	0.94	0.43
205	0.94	0.40
220	0.94	0.402

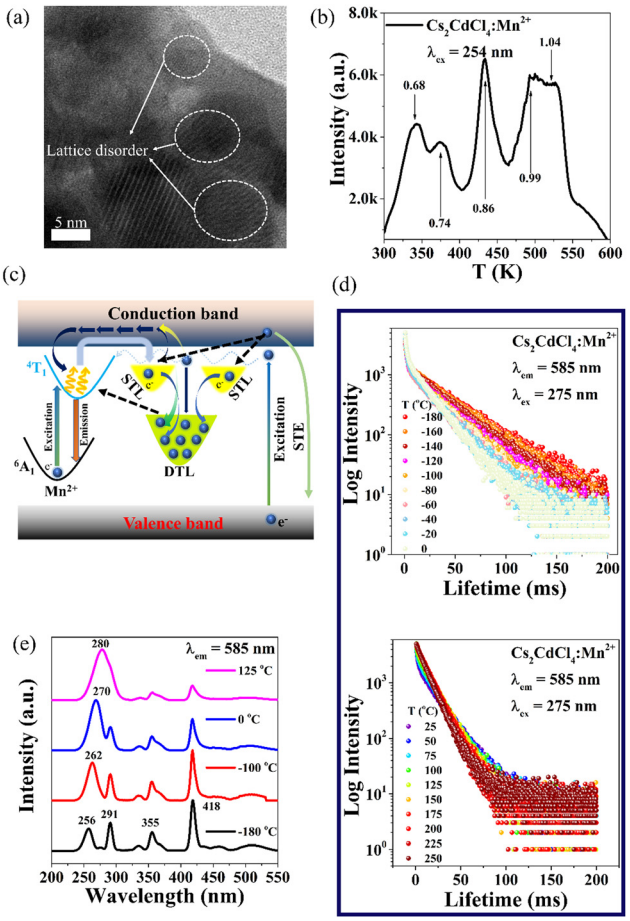

Fig. 5 (a) High-resolution TEM image of Cs_2CdCl_4:Mn^{2+}, where the lattice disorder induced by defects is marked by white arrows. (b) Thermoluminescence curve. (c) Configurational coordinate diagram. STL, shallow trap level; DTL, deep trap level. (d) Temperature-dependent decay curves of Mn^{2+}. (e) Temperature-dependent PLE spectra of Cs_2CdCl_4:Mn^{2+}.

1.04 eV. Fig. 5c shows several processes of electron transfer. Some of the excited electrons transfer to the excited state of Mn^{2+} at room temperature, enhancing the Mn^{2+} emission. Deep traps catch some of them. In addition, the shallow trap's electron component contributes to the Mn^{2+} emission, which boosts the Mn^{2+} emission. Deep traps have all captured the remaining electrons. Deep trap electrons have a key role in the emission of Mn^{2+} at high temperatures. The abnormal luminescence phenomena are caused by the electrons of deep traps obtaining energy to jump out of the deep trap and transfer to the excited state of Mn^{2+}. Such a host is unusual. A localized Cl vacancy trap energy level is created in the material's forbidden band through the addition of Mn^{2+}. When the temperature increases, the electrons bound by the trap energy level are de-trapped, reaching the excited state energy level *via* the conduction band and undergoing electron–hole complexation when returning to the ground state. The energy is emitted in the form of yellow emission to compensate for the weakened luminescence caused by the non-radiative transitions at high temperatures. When the two processes reach dynamic equilibrium, zero-thermal quenching can be achieved. Confirmed by the Jahn–Teller effect, slight distortions lead to

Table 3 Temperature-dependent decay times of Mn^{2+}

T (°C)	Decay time (ms)	T (°C)	Decay time (ms)
−180	12.95	25	17.65
−160	12.58	50	19.56
−140	11.90	75	21.16
−120	11.78	100	23.25
−100	11.26	125	26.52
−80	13.36	150	28.61
−60	13.62	175	30.81
−40	13.89	200	16.62
−20	14.36	225	15.84
0	14.51	250	15.43

easier STE formation due to the enhanced electron–phonon coupling (Fig. 5a). Secondly, the doping of Mn^{2+} introduces a large number of defect energy states, which is a basis for the enhanced STE phenomenon compared with the host. The trap states of the Mn^{2+} materials were calculated *via* the thermoluminescence spectrum, taking into account the Cl vacancies in the lattice, to further demonstrate that defects are involved in the process of anti-thermal quenching. The energy supplement process: the light irradiation at room temperature/high temperature makes these suitable defect states capture the excited carriers. The carriers trapped by the defect state will be released to the luminescence center under the influence of thermal disturbance as the temperature increases, making up for the energy loss enforced by the thermal quenching effect and enhancing the thermal stability of the luminous material.

We further demonstrated the process of energy transfer from STE to Mn^{2+} by monitoring the decay time of different emission peaks at different temperatures (Fig. 5d). The conclusion that all data can be explained using a double exponential decay model, $y = y_0 + A_1 \exp(-t/\tau_1) + A_2 \exp(-t/\tau_2)$, suggests that Cs_2CdCl_4:Mn^{2+} phosphors contain only a double light center (Table 3). By monitoring the excitation and emission spectra of Mn^{2+} at different temperatures, it is proved that energy transfer occurs between STE and Mn^{2+} at different temperatures (Fig. 5e). In addition, the decay time test further proves the energy transfer efficiency of Cs_2CdCl_4 and Mn^{2+}. The lifetime of Mn^{2+} increases with increasing temperature, which is strongly related to the material's deep traps. Partly as a result of energy transfer, the host's lifetime keeps getting shorter.

4. Conclusions

The corresponding defects that result from the substitution of Mn^{2+}-doped equivalent cations will also cooperate with the intrinsic defects to form functional trap energy levels to achieve a dynamic balance of carrier storage and response under external excitation, which will improve the luminescence performance of the material and even bring new luminescence properties. It has been clearly shown that the PL modulation is related to the density of surface trap states. We speculate that one possible reason for the observed PL enhancement is the reversible physical adsorption of oxygen, bromine and water.[49,50] Here, we aim to study the effect of Mn^{2+} doping on the photophysics of Cs_2CdCl_4, which is very beneficial to basic research. We demonstrate that Cl vacancy defects contribute to the luminescence enhancement of Cs_2CdCl_4:Mn^{2+} at high temperature. The understanding of Cl vacancy defects is still in its infancy. This work highlights the interaction between the introduction of Cl vacancies on Mn^{2+}-doped Cs_2CdCl_4 crystals and luminescence enhancement. These findings are helpful to understand the optical properties of Cs_2CdCl_4 materials measured at high temperature.

Conflicts of interest

There are no conflicts to declare.

Acknowledgements

This work is financially supported by the National Key Research and Development Program of China (2022YFB3503800), the National Natural Science Foundation of China (NSFC No. 51932009, 61205113, 51902226, 52172166, U2005212), the Natural Science Fund of Heilongjiang Province (LH2019F013), the 111 project (B13015) of Ministry Education of China to Harbin Engineering University, and the Fundamental Research Funds for the Central Universities (No. 3072020CF2520). Project of High-level Scientific Research Guidance of Harbin Engineering University (No. 3072022TS2508).

Notes and references

1 J. S. Manser, J. A. Christians and P. V. Kamat, *Chem. Rev.*, 2016, **116**, 12956–13008.
2 L. N. Quan, B. P. Rand, R. H. Friend, S. G. Mhaisalkar, T.-W. Lee and E. H. Sargent, *Chem. Rev.*, 2019, **119**, 7444–7477.
3 B. Saparov and D. B. Mitzi, *Chem. Rev.*, 2016, **116**, 4558–4596.
4 E. Shi, B. Yuan, S. B. Shiring, Y. Gao, Y. Guo, C. Su, M. Lai, P. Yang, J. Kong and B. M. Savoie, *Nature*, 2020, **580**, 614–620.
5 S. C. Erwin, L. Zu, M. I. Haftel, A. L. Efros, T. A. Kennedy and D. J. Norris, *Nature*, 2005, **436**, 91–94.
6 D. A. Berry, *Nature*, 2008, **454**, 692–693.
7 Y. Wang, T. Wu, J. Barbaud, W. Kong, D. Cui, H. Chen, X. Yang and L. J. S. Han, *Science*, 2019, **365**, 687–691.
8 D. J. Norris, A. L. Efros and S. C. Erwin, *Science*, 2008, **319**, 1776–1779.
9 D. Mocatta, G. Cohen, J. Schattner, O. Millo, E. Rabani and U. Banin, *Science*, 2011, **332**, 77–81.
10 M. V. Kovalenko, L. Protesescu and M. I. Bodnarchuk, *Science*, 2017, **358**, 745–750.
11 J. Hou, P. Chen, A. Shukla, A. Krajnc, T. Wang, X. Li, R. Doasa, L. H. Tizei, B. Chan and D. N. Johnstone, *Science*, 2021, **374**, 621–625.
12 Y. Wei, Z. Cheng and J. Lin, *Chem. Soc. Rev.*, 2019, **48**, 310–350.
13 E. Shi, Y. Gao, B. P. Finkenauer, A. H. Coffey and L. Dou, *Chem. Soc. Rev.*, 2018, **47**, 6046–6072.
14 M. D. Smith, B. A. Connor and H. I. Karunadasa, *Chem. Rev.*, 2019, **119**, 3104–3139.

15 X. Zhou, K. Han, Y. Wang, J. Jin, S. Jiang, Q. Zhang and Z. Xia, *Adv. Mater.*, 2023, 2212022.
16 B. Su, M. Li, E. Song and Z. Xia, *Adv. Funct. Mater.*, 2021, **31**, 2105316.
17 J. Jin, Y. Peng, Y. Xu, K. Han, A. Zhang, X.-B. Yang and Z. Xia, *Chem. Mater.*, 2022, **34**, 5717–5725.
18 Y. Jing, Y. Liu, X. Jiang, M. S. Molokeev, Z. Lin and Z. Xia, *Chem. Mater.*, 2020, **32**, 5327–5334.
19 B. Su, K. Han and Z. Xia, *J. Mater. Chem. C*, 2023, DOI: 10.1039/D2TC04249E.
20 M. Li and Z. Xia, *Chem. Soc. Rev.*, 2021, **50**, 2626–2662.
21 G. Zhou, B. Su, J. Huang, Q. Zhang and Z. Xia, *Mater. Sci. Eng., R*, 2020, **141**, 100548.
22 K. Han, J. Jin, B. Su and Z. Xia, *Trends Chem.*, 2022, **4**, 1034–1044.
23 B. Su, G. Zhou, J. Huang, E. Song, A. Nag and Z. Xia, *Laser Photonics Rev.*, 2021, **15**, 2000334.
24 Y. Jing, Y. Liu, M. Li and Z. Xia, *Adv. Opt. Mater.*, 2021, **9**, 2002213.
25 B. Zhao, S. Bai, V. Kim, R. Lamboll, R. Shivanna, F. Auras, J. M. Richter, L. Yang, L. Dai and M. J. N. P. Alsari, *Nat. Photonics*, 2018, **12**, 783–789.
26 T. Chiba, Y. Hayashi, H. Ebe, K. Hoshi, J. Sato, S. Sato, Y.-J. Pu, S. Ohisa and J. J. N. P. Kido, *Nat. Photonics*, 2018, **12**, 681–687.
27 Z. Yuan, C. Zhou, Y. Tian, Y. Shu, J. Messier, J. C. Wang, L. J. van de Burgt, K. Kountouriotis, Y. Xin, E. Holt, K. Schanze, R. Clark, T. Siegrist and B. Ma, *Nat. Commun.*, 2017, **8**, 14051.
28 X. Yang, X. Zhang, J. Deng, Z. Chu, Q. Jiang, J. Meng, P. Wang, L. Zhang, Z. Yin and J. You, *Nat. Commun.*, 2018, **9**, 1–8.
29 R. N. Bhargava, D. Gallagher, X. Hong and A. Nurmikko, *Phys. Rev. Lett.*, 1994, **72**, 416–419.
30 J. P. Perdew, K. Burke and M. Ernzerhof, *Phys. Rev. Lett.*, 1996, **77**, 3865–3868.
31 J. Shamsi, A. S. Urban, M. Imran, L. De Trizio and L. Manna, *Chem. Rev.*, 2019, **119**, 3296–3348.
32 A. Zhang, Y. Liu, G. Liu and Z. Xia, *Chem. Mater.*, 2022, **34**, 3006–3012.
33 Y. Liu, A. Nag, L. Manna and Z. Xia, *Angew. Chem., Int. Ed.*, 2021, **133**, 11696–11707.
34 Y. Liu, X. Rong, M. Li, M. S. Molokeev, J. Zhao and Z. Xia, *Angew. Chem., Int. Ed.*, 2020, **59**, 11634–11640.
35 Y. Jing, Y. Liu, J. Zhao and Z. Xia, *J. Phys. Chem. Lett.*, 2019, **10**, 7439–7444.
36 Y. Liu, Y. Jing, J. Zhao, Q. Liu and Z. Xia, *Chem. Mater.*, 2019, **31**, 3333–3339.
37 J. Zhou, Z. Xia, M. S. Molokeev, X. Zhang, D. Peng and Q. Liu, *J. Mater. Chem. A*, 2017, **5**, 15031–15037.
38 K. Han, J. Qiao, S. Zhang, B. Su, B. Lou, C. G. Ma and Z. Xia, *Laser Photonics Rev.*, 2023, **17**, 2200458.
39 M. D. Smith, B. A. Connor and H. I. Karunadasa, *Chem. Rev.*, 2019, **119**, 3104–3139.
40 B. Vargas, G. Rodriguez-Lopez and D. Solis-Ibarra, *ACS Energy Lett.*, 2020, **5**, 3591–3608.
41 X. Li, J. M. Hoffman and M. G. Kanatzidis, *Chem. Rev.*, 2021, **121**, 2230–2291.
42 S. N. Ruddlesden and P. Popper, *Acta Crystallogr.*, 1957, **10**, 538–540.
43 S. Siegel and E. Gebert, *Acta Crystallogr.*, 1964, **17**, 790.
44 T. Sakai, M. Koshimizu, Y. Fujimoto, D. Nakauchi, T. Yanagida and K. Asai, *Sens. Mater.*, 2018, **30**, 1565–1575.
45 F. Locardi, M. Samoli, A. Martinelli, O. Erdem, D. V. Magalhaes, S. Bals and Z. Hens, *ACS Nano*, 2021, **15**, 17729–17737.
46 Y. Liu, J. Zhang, B. Han, X. Wang, Z. Wang, C. Xue, G. Bian, D. Hu, R. Zhou, D. Li, Z. Wang, Z. Ouyang, M. Li and T. Wu, *J. Am. Chem. Soc.*, 2020, **142**(14), 6649–6660.
47 S. He, Q. Qiang, T. Lang, M. Cai, T. Han, H. You, L. Peng, S. Cao, B. Liu, X. Jing and B. Jia, *Angew. Chem., Int. Ed.*, 2022, **134**, e202208937.
48 F. Urbach, *Sitzungsberichte Akad. Der Wiss*, 1930, **139**, 363–372.
49 Y. Wang, Y. Ren, S. Zhang, J. Wu, J. Song, X. Li, J. Xu, C. H. Sow, H. Zeng and H. Sun, *Commun. Phys.*, 2018, **1**, 96.
50 H.-H. Fang, S. Adjokatse, H. Wei, J. Yang, G. R. Blake, J. Huang, J. Even and M. A. Loi, *Sci. Adv.*, 2016, **2**, e1600534.

